OPEN ACCESS
IOP Publishing
Superconductor Science and Technology
Supercond. Sci. Technol. **36** (2023) 115025 (11pp)
https://doi.org/10.1088/1361-6668/acfbfc

MOSFET-based HTS flux pump

Róbert Jurčo[1,2,*], **Anna Vaskuri**[1], **Benoit Curé**[1], **Alexey Dudarev**[1] and **Matthias Mentink**[1]

[1] CERN, 1211 Geneva 23, Switzerland
[2] Faculty of Mathematics and Physics, Charles University, Ke Karlovu 3, 121 16 Praha 2, Czech Republic

E-mail: robert.jurco.1@gmail.com

Received 10 May 2023, revised 11 September 2023
Accepted for publication 21 September 2023
Published 9 October 2023

Abstract

We have developed a high-temperature superconducting (HTS) flux pump using high-power metal-oxide-semiconductor field-effect transistors (MOSFETs) for switching. For its primary coil, two commercial transformers are utilized, each consisting of two copper coils wound on a single iron core, which enables changing the load current over primary current ratio (101 or 194) between the primary and secondary coils. Full-wave rectification is achieved with two half-wave secondary circuits, each of them having six HTS one-turn coils to lower the resistance. Each secondary coil is composed out of nickel-reinforced BSCCO tapes, where 12 MOSFETs have been soldered in parallel straight to the tapes and controlled with analog electronics. Secondary coils are clamped to custom-made copper-stabilized HTS current leads. A support structure for keeping the HTS coils in place was 3D-printed using cryogenic-compatible composite material PETG-CF20. Resistances of the two secondary circuits were measured to be 4 $\mu\Omega$ and 7 $\mu\Omega$ at 77 K with a total critical current of 980 A. We successfully ramped up a 50 μH Conductor on Round Core solenoid at 77 K using our HTS flux pump with 50 Hz AC voltage source. We achieved a maximal load current of 900 A and exceeded the 715 A critical current of the solenoid. During the thermal runaway of the magnet, the increased load voltage limits the maximum load current supplied by the flux pump.

Keywords: HTS, flux pump, transformer-rectifier, MOSFET, superconducting magnet

(Some figures may appear in colour only in the online journal)

1. Introduction

Flux pumps are these days a commonly studied topic given their significance in operational energy-savings. With traditional room-temperature operated power supplies significant cryogenic power is needed for powering high-current superconducting detector magnets while maintaining the superconducting state. For example, the ATLAS magnets, which features three superconducting toroidal-shaped magnets each powered at 20.4 kA and one superconducting solenoid powered at 7.73 kA, all powered from room-temperature power converters, require 3 kW of cooling power at 4.5 K to maintain superconductivity at the bottom of each lead [1], with an associated cryogenic power consumption and water-cooling requirement at room temperature of about 900 kW. With a superconducting flux pump the need for high current flowing from room temperature is avoided, and therefore it may contribute to lowering the operational power consumption of future detector magnets. For this purpose, it is a technology that is being investigated in the context of the CERN EP R&D program.

The first superconducting flux pumps date back to the 1960s. Flux pumps with different switching methods were thoroughly analyzed in 1981 by van de Klundert and ten Kate [2, 3]. This was followed by the first successful implementations of a flux pump as a DC current source in magnetic systems of nuclear detectors. A successful example is the powering of the CMD-2 detector at the Budker Institute of Nuclear Physics in Russia [4], which was in operation from 1989 to at

* Author to whom any correspondence should be addressed.

least 1999. This case demonstrated that superconducting flux pumps are a reasonable option for powering superconducting magnets for particle detectors. The largest possible current that was achieved using a low-temperature superconducting (LTS) flux pump was 60 kA [5] achieved by using thermally regulated LTS switches, consisting of a heater element that was in thermal contact with the LTS cable. This LTS flux pump used helium cooling but the exact operation temperature was not mentioned in the paper.

An overview of flux pumps for high-temperature superconducting (HTS) coils is provided by [6, 7]. Most of these HTS flux pumps fall into the following two categories: travelling wave flux pumps or transformer-rectifier flux pumps. Travelling wave flux pumps, where the travelling wave is generated by linear windings, were originally proposed in [8, 9] with recent contributions in [10–13]. Travelling wave flux pumps also include HTS dynamo flux pumps [14, 15]. With the last mentioned method, the highest current of 700 A was achieved in 2018 [15]. The transformer-rectifier flux pumps can be divided into categories based on the method of switching, which are dynamic resistance switches [16, 17], overcurrent switches [18, 19] and other new types of switches [20, 21]. The first successful demonstration of an HTS flux pump based on metal-oxide-semiconductor field-effect transistors (MOSFETs) took place in 2005 [22]. The study focused on the ability of the flux pump to supply a DC current of 63 A at 15 K into a load magnet, but the study did not address system losses. The highest current obtained by the HTS flux pump was >2 kA (published in 2020 [19]) and was based on a self-switching rectifier.

In this work, we demonstrate and evaluate the feasibility of using an MOSFET-based HTS flux pump to charge a magnet at 77 K with minimal power consumption. The MOSFET-based design, where MOSFETs are soldered straight to HTS tapes, offers several advantages over other types of flux pumps, including faster switching time, operation at elevated temperatures, and a simpler and more robust control system. The inclusion of a large number of parallel MOSFETs and parallel secondary coils ensure that the flux pump continues to power the load even if one of them fails. As a result, this design is suitable for powering particle detector magnets in space where maintenance and repair can be challenging.

2. Design and construction of the HTS flux pump

When designing a MOSFET-based HTS flux pump, our goal was to minimize resistive losses and maximize the load current. Therefore, we use a full-wave transformer rectifier principle according to figure 1. We selected a high load current over the primary current ratio ($I_{\mathrm{load}}/I_{p,\mathrm{rms}}$) and used multiple secondary coils to increase the critical current of the system. We soldered the MOSFETs directly to the HTS tapes that form the secondary coil of the flux pump, which results in lower resistance in comparison to using a separate compartment for MOSFETs.

The flux pump design presented in figure 2 comprises primary and secondary coils that are mounted on a support

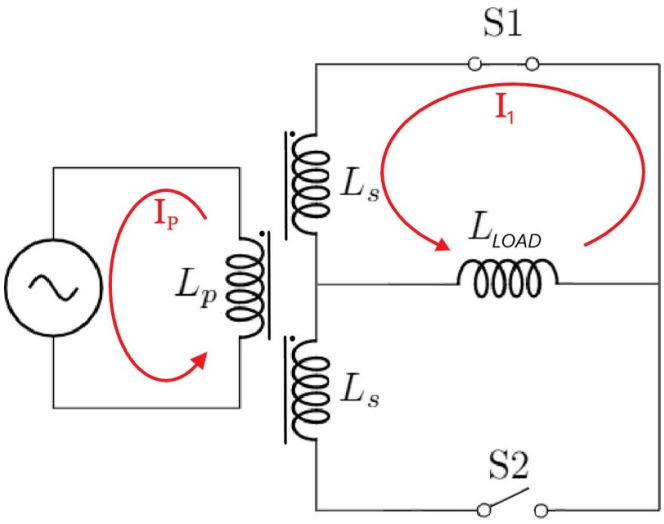

Figure 1. Electrical schematic of flux pump during charging of a load magnet.

structure made of 3D-printed PETG-CF20 (80% PETG, 20% carbon fiber). We chose this material based on the research of Klaassen [23], which demonstrated that certain 3D-printed plastics can be used as support structures in cryogenic applications. PETG-CF20 has a thermal contraction coefficient in the printing direction that matches that of copper, ensuring mechanical compatibility with our coils. The toroidal shape confines the flux minimizing the stray magnetic field of the flux pump. A modular design is achieved by using multiple secondary coils that are clamped to copper leads with copper clamps which can be seen in figures 2(b) and (c). This enables a quick and easy replacement of the secondary coils in the event of a malfunction.

2.1. Primary coil

The primary coil was constructed from two open type toroidal transformers. Each transformer comprised two primary and two secondary coils made of copper, but only the primary ones were utilized. This resulted in four primary coils in total, each pair wound on a common iron core. In general, the purpose of an iron core is to improve the coupling between the primary and secondary coils. However, if the flux pump is operated in an external magnetic field, the iron core may saturate reducing the coupling efficiency. These primary coils can be arranged in two practical configurations: either all in parallel (P) with the measured $I_{\mathrm{load}}/I_{p,\mathrm{rms}} = 101$ or coils of each pair in parallel and then pairs together in series (PS) with the measured $I_{\mathrm{load}}/I_{p,\mathrm{rms}} = 194$. The P configuration had a net inductance that was $1/4$ of that of the PS configuration. The net inductance was dependent on the current due to the heating of the iron core since the magnetic permeability of iron has a strong temperature dependence [24]. Each transformer had the following properties [25]: 8.4 kg mass, 175 mm outer radius, 70 mm inner radius, 85 mm height and 76 mΩ resistance for a single primary coil at 77 K. Both primary coils were enclosed by 3D-printed PETG-CF20 support parts according to figure 2(a).

Two identical support parts sealed the opposite side of each coil and a middle support sealed coil from the common side with a thin layer of PETG-CF20 in between the coils.

2.2. Secondary coil

Both secondary circuits in figure 1 consist of six coils made of two nickel-reinforced BSCCO tapes with 12 parallel MOSFETs soldered between them as a switch. The location of the BSCCO tapes and the MOSFETs are shown in figure 2(b) and the arrangement of the MOSFETs between the BSCCO tapes is shown in figure 3. We chose nickel-reinforced BSCCO tapes for their durability. The ReBCO (Rare-earth Barium Copper Oxide) tapes would have been damaged by clamping them onto the copper leads (rings). The BSCCO tapes had a critical current of 164 A at 77 K, giving the flux pump a critical current of 984 A at 77 K. The MOSFETs were surface mount IRL40SC228, *n*-type, with the maximum voltage and current thresholds of 40 V, 360 A at room temperature. The on-state resistance of one MOSFET at 77 K was 234 $\mu\Omega$ [26]. Thus, the expected resistance of a single secondary coil at 77 K (12 MOSFETs) was 19.5 $\mu\Omega$ and the expected resistance of one secondary circuit at 77 K (72 MOSFETs) was 3.25 $\mu\Omega$. The measured resistances of the secondary circuits were 4.2 $\mu\Omega$ and 6.5 $\mu\Omega$. The difference was due to the copper ring electrical resistance between adjacent secondary coils, as shown in figure 2. We soldered the MOSFETs on the HTS tapes by securing the HTS tapes on the hot plate with adhesive tape, heating them to 175 °C, melting low-temperature solder on the tape surface and placing the MOSFETs on the solder. Then, we waited for the hot plate to cool down before removing the finished secondary circuit. The solder used was a solder wire (ChipQuik SMDIN52SN48) containing 52% indium and 48% tin with a melting temperature of 118 °C.

2.3. Copper-stabilized HTS current leads for attaching the secondary coils

The current from each secondary coil is collected by the copper rings. To reduce the heat load, we soldered ReBCO tape stacks of four around them in two rows. These copper-stabilized HTS cables were soldered using a method developed by Vaskuri *et al* in [27]. We layered the ReBCO tapes together with a low-temperature solder and then compressed them with a Teflon tube attached to the Kapton tape (see figure 4(a)). The ReBCO tapes were soldered to the copper rings in an oven for 6 hours at 180 °C. The secondary coils were then clamped at their ends to the current leads using blocks of copper and indium foil.

The secondary coils are clamped to the copper ring and the HTS tape soldered to it can be seen in figures 4(b) and (c).

As mentioned earlier, the flux pump has two secondary circuits with opposite coupling directions to the primary coil. In our case, we achieved this by connecting half of the secondary coils (that is, one of the secondary circuits) to the output of the flux pump in the opposite direction. The copper rings were designed so that they exchange their arrangement for half of

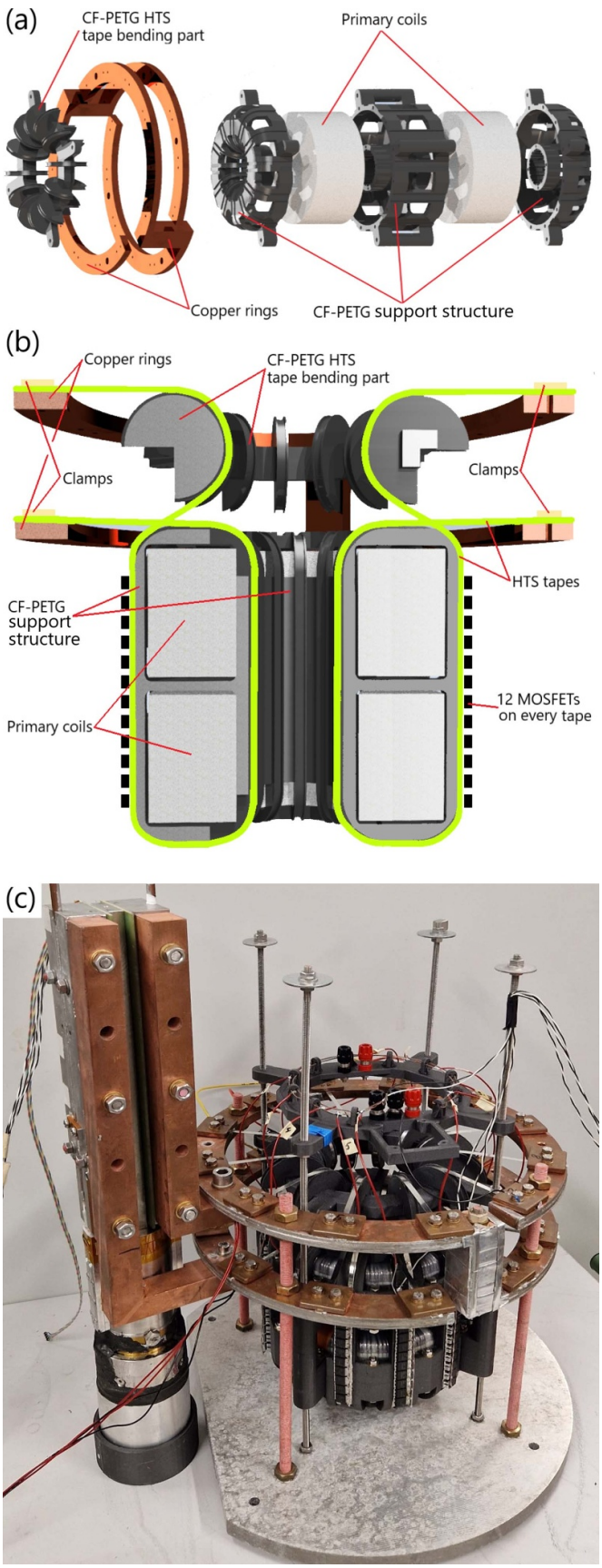

Figure 2. Assembly of the MOSFET-based HTS flux pump (a), winding configuration of the secondary coils (b), and the constructed flux pump with a load magnet connected (c).

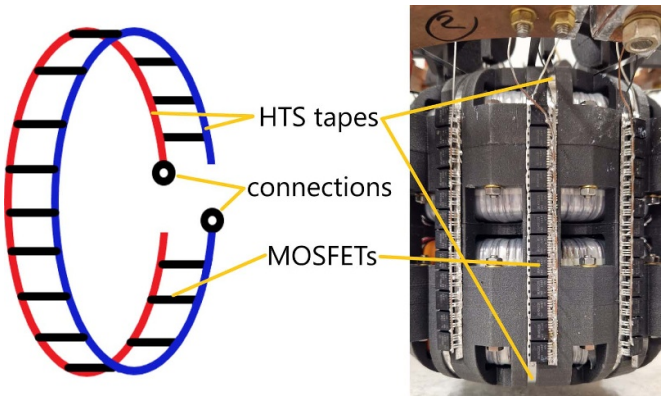

Figure 3. One secondary coil composed of two HTS tapes between which MOSFETs are soldered.

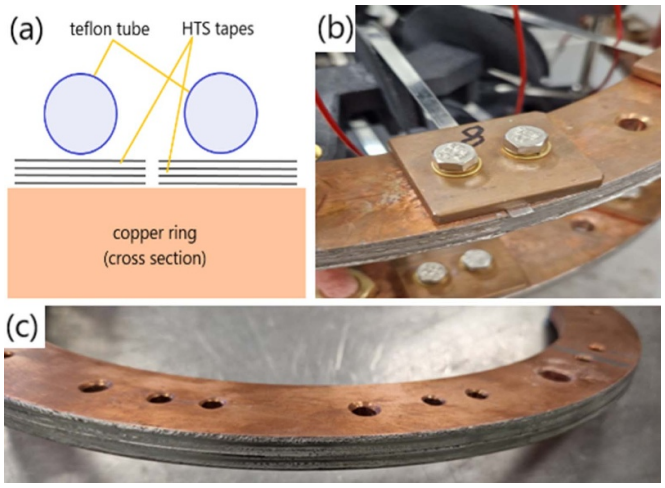

Figure 4. (a) Soldering of ReBCO tapes to the copper rings: layers of HTS tapes were compressed by Teflon tubes along the outer perimeter of copper rings and soldered using the method described in [27]. (b) A nickel-reinforced BSCCO tape (secondary coil) clamped to the copper ring. (c) Layers of ReBCO tapes soldered around the copper ring.

the secondary coils (figure 2). A 3D-printed bending part was used to safely bend the HTS tapes. The flux pump was supported by an aluminum flange that allowed us to connect it to the cryostat insert. To connect to the support flange, we used steel rods to connect 3D-printed parts and fiberglass rods to connect copper rings.

2.4. Control circuit

The MOSFETs are controlled by an analog circuit composed of operational amplifiers that amplify the voltage V_{DS} across the drain and source of the MOSFETs. A schematic representation of a full-wave flux pump controlled by operational amplifiers (Op-Amps) is presented in figure 5. MOSFETs become more efficient at gate voltages higher than the threshold voltage that increases towards cryogenic temperatures, and therefore 15 V was used to close the MOSFETs. To achieve fast switching and low losses, the measured voltage V_{DS} was amplified by Op-Amp in an open loop configuration, which

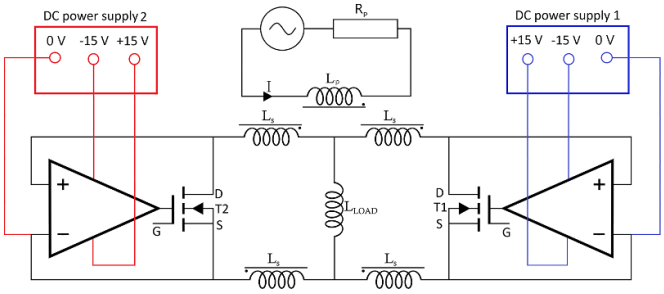

Figure 5. Full-wave transformer rectifier (flux pump) where the gate voltages of the MOSFETs are controlled by operational amplifiers.

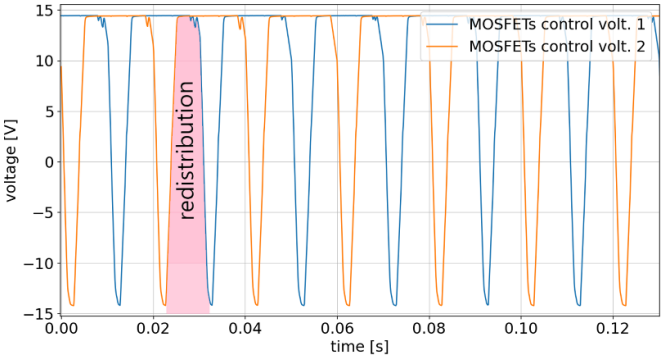

Figure 6. Control voltage V_{GS} obtained by amplifying voltage V_{DS} across MOSFETs during ramp-up of the load magnet.

means that the Op-Amp is operated as a comparator. We chose rail-to-rail Op-Amps by Analog Devices (OP27GPZ) with a low offset and drift, and an open-loop gain $A_{vo} = 1.5 \cdot 10^6$.

In figure 6 we can see control signals during ramp-up of the load magnet. The flux pump switches between the charging and redistribution phase (see appendix). In the charging phase, the load current increases in one secondary circuit. In the redistribution phase, the currents are enclosed in their individual secondary circuits, while the load current (constant when no losses) is given by their difference. The overlap between the gate voltages in figure 6 corresponds to the current redistribution.

During testing, we verified that the MOSFETs remain open when a negative gate voltage is applied. The control board was placed outside of the cryostat, as it cannot handle cryogenic temperatures.

3. Powering an HTS magnet

A CORC (Conductor on Round Core [28]) solenoid built by Mulder *et al* [29] was used to test the functionality of the flux pump. The solenoid is made of a superconducting CORC cable, which is a high-current ReBCO cable composed of multiple tapes. At 77 K, the solenoid has an inductance of 49.74 μH and a critical current of 715 A. To avoid introducing additional resistive losses in the secondary circuits, we placed a Hall-probe in the middle of the solenoid for contactless current measurement with a calibrated sensitivity of 18.9 μV A^{-1}. The

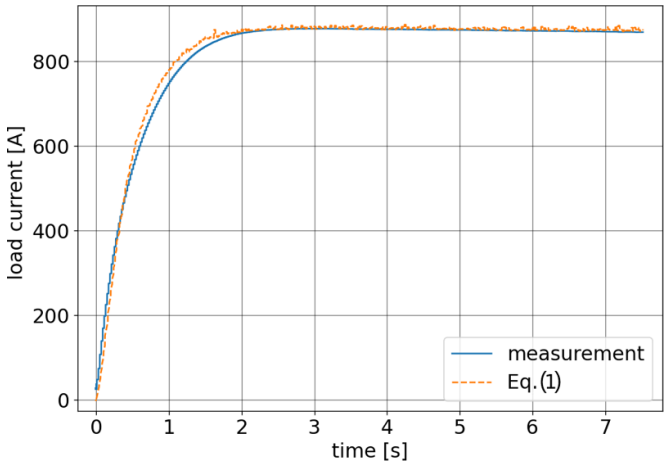

Figure 7. Measured evolution of the load current (RMS) and the theoretical charging by equation (1).

probe used was HHP-NA manufactured by AREPOC s.r.o., Slovakia. The CORC solenoid was connected to the flux pump using copper current leads with a combined resistance of 5.96 $\mu\Omega$.

3.1. Analysis of the ramping

To power a primary coil, a variable transformer was used, where the maximum applied voltage to the primary coil was always kept well below 50 V (50 Hz). To acquire data, an 8-channel DAXUS DXS-100 oscilloscope was used to record RMS voltages and currents across the primary coil (V_p, I_p) and across the CORC solenoid (V_{load}, I_{load}). The measured data are shown in figure 7 along with their fits. To fit the data of solenoid ramping, we derived a relation (see appendix) between load and primary current as

$$I_{\text{load}}(t) = \frac{\sqrt{2}\, I_{p,\text{rms}}(t)\, M}{L_s}\left(1-\cos(\omega\tau_r)\right) \cdot \left[1-\left(\frac{L_{\text{load}}}{L_s+L_{\text{load}}}\right)^{2ft}\right] \tag{1}$$

using the fitted primary inductance ($L_p = 0.02$ H), secondary inductance ($L_s = 2.7\,\mu$H), and coupling coefficient ($k = 0.795$), giving us $M = 185\,\mu$H. The redistribution time $\tau_r = 5$ ms was determined from the steady-state measurements discussed in section 3.2. We may notice that L_p is much lower than expected. This is because the iron core gets saturated and hence does not affect the inductances anymore. The coupling k is then proportional to the ratio of secondary and primary coils cross sections. It should be noted that the measured RMS primary current $I_{p,\text{rms}}(t)$ is non-constant because a voltage source was used instead of a current source. This has been accounted for in the evaluation of equation (1) in figure 7. We also note that in the case of no losses in the secondary circuits, $\tau_r = 10$ ms, the achieved load current would be twice larger.

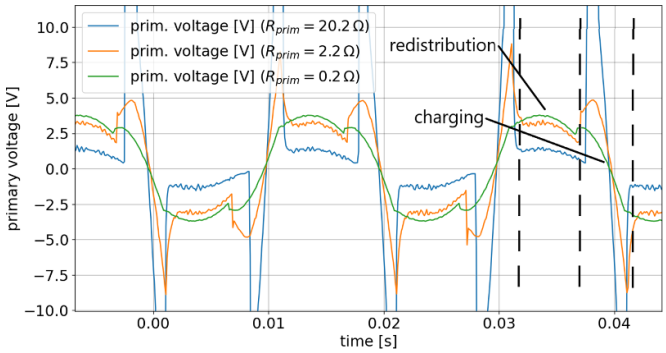

Figure 8. Measured primary voltage waveforms with varying series resistor value connected in the primary circuit.

3.2. Steady-state measurements

The CORC solenoid was ramped up to various currents in the range between 200 A and 900 A. The same oscilloscope was used to record voltage and current across the primary coil (V_p, I_p), across the CORC solenoid (V_{load}, I_{load}), and across both sets of MOSFETs and gate voltages. The values recorded were instantaneous voltages. The primary current was measured with a shunt of 0.2 Ω, and the load current with the Hall probe calibrated for contactless current measurement. Each measurement was taken at a sampling rate of 10 kHz for a duration of 2 s and then averaged.

We created a voltage divider by connecting an additional resistor into the primary circuit to achieve finer voltage settings from the voltage source. We observed that the measured waveform of the primary voltage strongly depends on the resistance of the primary circuit (see figure 8). To reduce the distortion from a sine wave, we chose a 2 Ω resistor. The primary resistance also influenced the redistribution time: it was $\tau_r \approx 5.5$ ms for a 20 Ω shunt and $\tau_r \approx 5$ ms for a 2 Ω shunt, respectively. The longer redistribution time for higher shunt resistances might be due to more power being added to the circuit during charging and less power being available for current redistribution.

We measured a non-linear transition around 700 A which coincides with the critical current of 715 A of the CORC solenoid at 77 K. Therefore, for analysis we use linear fits of data only below 700 A. In figure 9, we can see linear fits of I_{load} for both primary coil arrangements.

Using the ratio $I_{\text{load}}/I_{p,\text{rms}} = 101$ obtained from figure 9 and redistribution time $\tau_r = 5$ ms we can obtain the ratio of mutual and secondary inductances M/L_s using the equation (for details see equation (A.12) in appendix)

$$\frac{M}{L_s} = \frac{I_{\text{load}}}{I_{p,\text{rms}}}\frac{1}{\sqrt{2}\left(1-\cos(\omega\tau_r)\right)} = 71.4\,. \tag{2}$$

We can compare this with the results obtained from the fit in figure 7 which gives us $M/L_s = 68.5$. Despite exceeding the critical current of the CORC solenoid, thus driving it to be partially normal-conducting, we achieved a maximum load current over 900 A. However, if we use helium vapors instead of liquid nitrogen to cool down the flux pump to 50 K, we

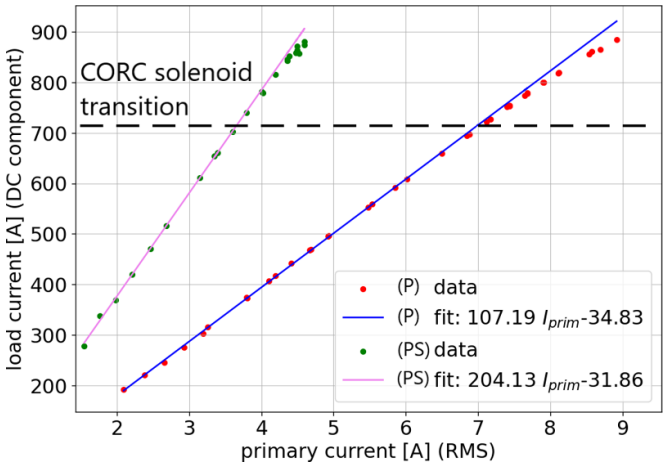

Figure 9. Steady-state measurements of load current levels as a function of the primary current levels together with their linear fits. $I_{\mathrm{load}}/I_{p,\mathrm{rms}}$ ratios obtained are 101 for P configuration and 194 for PS configuration. The $I_{\mathrm{load}}/I_{p,\mathrm{rms}}$ ratio for PS configuration is less than double from that of P configuration probably due to the complex wiring.

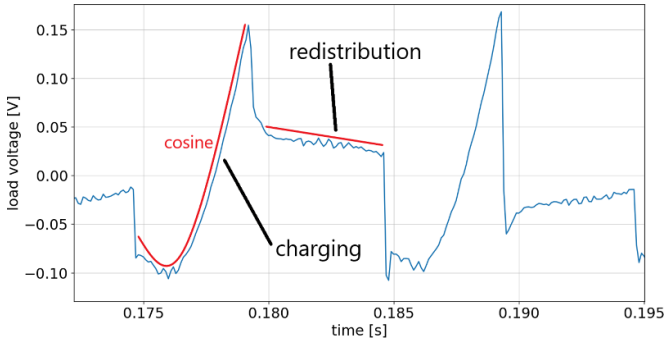

Figure 10. Load voltage characteristics measured during the steady-state operation.

would achieve much higher currents since the HTS tapes having higher critical current at lower temperatures [30, 31] and although the resistance of the MOSFETs increases at temperatures lower than 100 K, their resistance is still low around 50 K [26].

Steady state consists of two periodic events: charging and redistribution, repeating at twice the frequency of the primary current. The load voltage is close to zero during redistribution. From its deviation from zero, we can determine the redistribution time constant. This is defined as the time in which the current being redistributed (or voltage across MOSFETs) drops to half of its value. The evolution of load voltage during charging behaves as

$$V_{\mathrm{load}}(t) = \frac{ML_{\mathrm{load}}}{L_s + L_{\mathrm{load}}} \frac{\mathrm{d}I_p(t)}{\mathrm{d}t}\ , \tag{3}$$

$$V_{\mathrm{load}}(t) = \frac{ML_{\mathrm{load}}I_0}{L_s + L_{\mathrm{load}}} \cos(\omega t - \phi)\ , \tag{4}$$

where the primary current is $I_p(t) = -I_0\cos(\omega t)$ for $t \in (\tau_r, \pi/\omega)$. For details see equation (A.22) in appendix. Here, τ_r represents a moment when the current stops redistribution between the secondary circuits and ϕ represents the phase shift between the voltage and current. The phase shift is chosen so that the magnetic flux changes its direction each $t = \pi/\omega$. The behavior of the load voltage can be seen in figure 10. Here we see almost zero voltage during redistribution, as there is supposed to be no change in load current and cosine behavior during charging. From this plot, it is possible to determine the phase shift $\phi = 1.1$ rad and redistribution time $\tau_r = 5.5$ ms. However, it is much easier to determine the phase shift straight from the offset of the primary voltage with respect to the primary current and to determine the redistribution time τ_r from the gate voltages.

3.3. Power losses

Figures 11(a) and (b) show how the absolute power is dissipated inside the system. The power of the primary coil and the power of the CORC solenoid were obtained by averaging over the voltage and current waveform data recorded with a 10 kHz sampling frequency and the power dissipated in the resistive components was calculated using RI^2. Figures 11(a) and (b) show that the input power of the system is approximately equal to the power dissipated inside the CORC solenoid together with the resistive losses inside the primary coil and MOSFETs, within the relative deviation plotted in figures 11(c) and (d). This means that the power dissipated as heat inside the iron core due to hysteresis and Eddy currents is only a few percent of the total power consumption. The power consumption is nonlinear, with a typical total dissipation in the flux-pump of just under 6 W at 800 A. Comparing figures 11(a) and (b), we observe that the power output for both $I_{\mathrm{load}}/I_{p,\mathrm{rms}}$ ratio configurations is equal until the moment the CORC solenoid quenches. After exceeding the critical current of the CORC solenoid, the power inside the solenoid is lost to heat since the HTS cable of the CORC magnet is passively protected with normal metal. However, the power dissipated inside MOSFETs and primary coil behaves similarly, regardless of the behavior of the CORC solenoid.

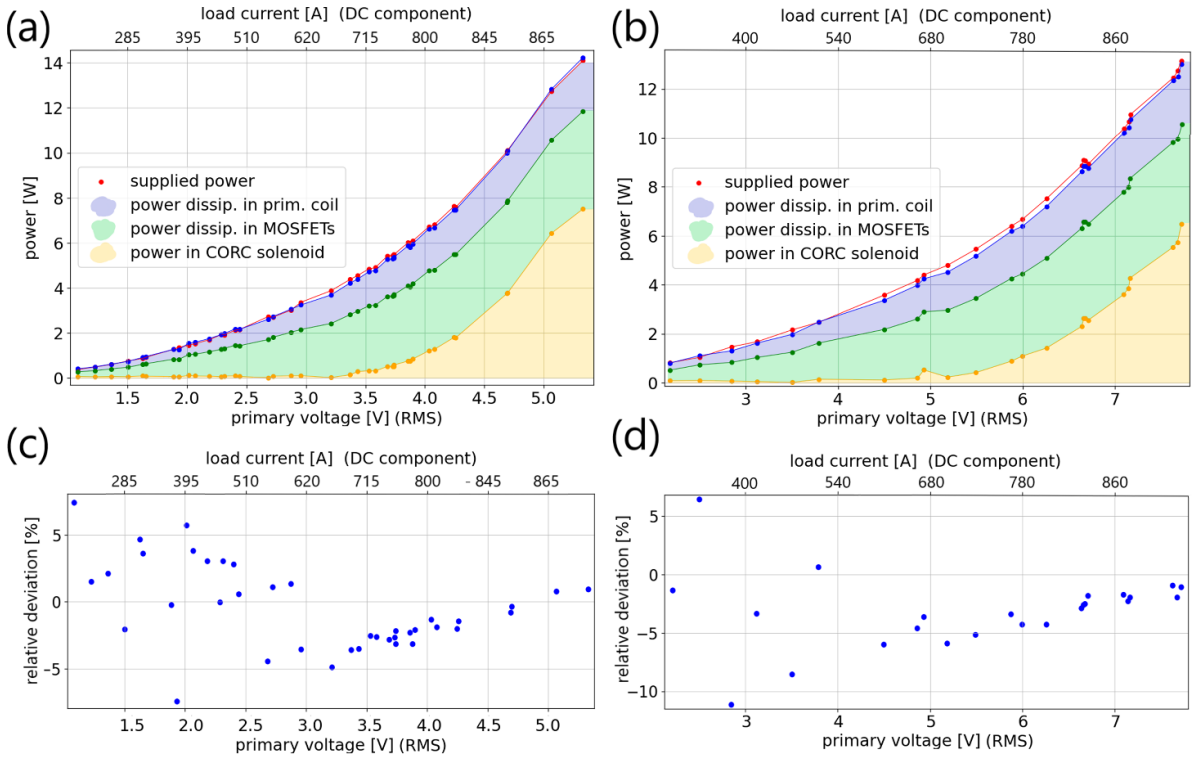

Figure 11. Absolute power distribution in the system for the primary coil arrangement P (a) and PS (b), and the corresponding relative deviations between the supplied power and output power for the primary coil arrangement P (c) and PS (d).

3.4. Transient load current behavior during a magnet quench or lost primary power

In figure 12(a), we can see that charging of the magnet above the critical current caused it to quench. A thermal runaway does not occur immediately at 715 A as the CORC solenoid was submerged in liquid nitrogen, thus providing good cooling conditions, and as the flux pump is not able to provide enough power to overcome the extra losses. However, above 900 A, the flux pump itself gets close to its own critical current and the CORC solenoid starts to develop significant resistance due to a thermal runaway. To be able to again reach high currents, we need to first switch off the flux pump and also DC power supplies of the MOSFETs to give the CORC solenoid some time to cool down.

In our setup, the thermal runaway does not destroy the flux pump because the energy stored inside the CORC solenoid (20 J at 700 A) is not enough to damage the HTS tapes. As the HTS tapes turn resistive, the flux pump is not able to provide enough power to damage them. This can also be seen in the fact that the flux pump is able to power only superconducting magnets with minimal losses. With a larger superconducting magnet having a higher stored energy an additional protection circuitfor example, based on diodes, would be needed to safely discharge the magnet.

In figure 12(b), we can see load current of the CORC solenoid in case of power loss at $t \approx 4$ s. The exponential decrease in the load magnet is caused by the resistance of the current leads, copper rings and clamps. The voltage across the MOSFETs keeps them closed during the power loss. The delay of current in the secondary circuit after switching off the primary power of the flux pump (figure 12(b)) is fitted with an exponential function $I_{\mathrm{load}} \cdot \exp\left(-\left(t-t_0\right)/\tau\right)$, where $\tau = L/R$, giving a time constant of 10 s. While the resistance of the secondary circuit changes due to reduced heat load of the copper parts and due to the load magnet transitioning fully superconductive as the load current decays, this corresponds to an effective resistance of about 5 $\mu\Omega$.

4. Discussion

With the HTS flux pump introduced in this work, we achieved a maximal load current of 900 A in liquid nitrogen at 77 K. However, if we would use helium vapors or cryocoolers instead of liquid nitrogen to cool the flux pump down to 50 K, theoretically we should be able to reach a load current of 3.6 kA [30, 31].

With the 50 μH load magnet the time constant after switching off the flux pump was 10 s. Flux pump is a much more viable option for high inductance superconducting magnets, as the time constant would be on the order of hours. This would allow one to switch off the flux pump once the nominal load current is reached and only switch it on occasionally, if necessary, to top up the load current.

While operating the system, we noticed iron core saturation, and thus the next HTS flux pump version should have an air core. To further reduce the overall power consumption

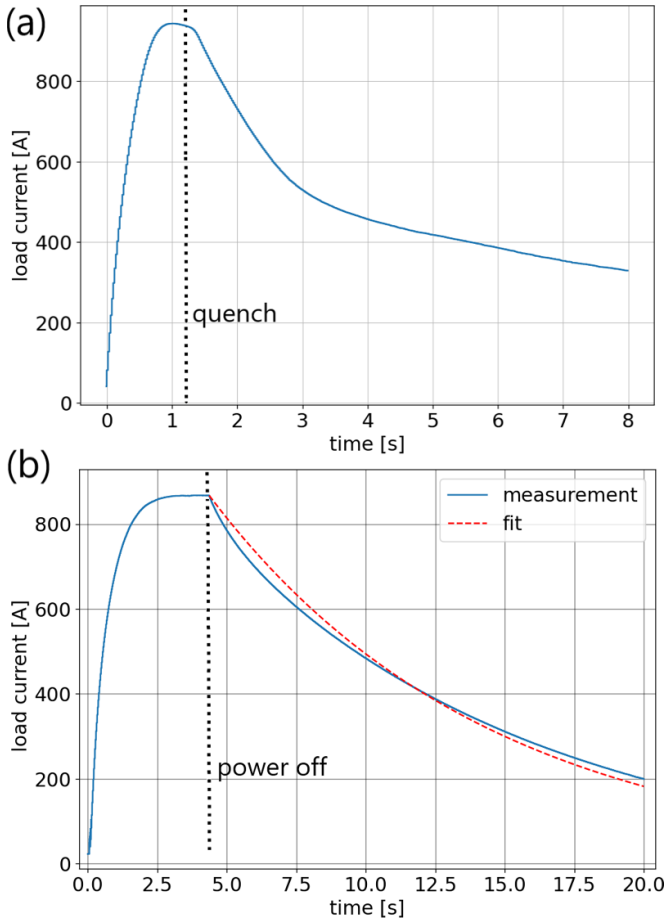

Figure 12. (a) Recorded quench of the magnet and flux pump. (b) Measured load current decay when the AC voltage source of the flux pump is switched off at $t \approx 4$ s.

of the flux pump, the next version should also have a primary coil made of HTS. In the future it would be better to use current sources for an easier comparison with theory.

5. Summary

This study demonstrates that MOSFET based HTS flux pumps are a feasible and reliable option to power up a superconducting magnet with minimal losses. We show that soldering MOSFETs straight to HTS tapes is a viable option for making secondary coils of an HTS flux pump. We demonstrate the HTS flux pump concept by achieving a maximal load current of 900 A at 77 K.

We analyzed the power losses and found that losses were mainly due to resistive heating in the primary coil and in the MOSFETs. Higher efficiency could be achieved by using a superconducting primary coil and by soldering more parallel MOSFETs to each secondary coil. We also show that the flux pump is not damaged by a quench in the system when 50 μH HTS magnet is connected as a load. With this load magnet the measured time constant after switching off the flux pump is 10 s. With higher inductance load magnets, a diode or transistor based protection circuit is needed in parallel with the magnet, to keep the induced voltage at a safe level during a thermal runaway.

Data availability statement

All data that support the findings of this study are included within the article.

Acknowledgment

The authors thank Dr Tim Mulder for useful discussions and for providing the measured properties of the CORC magnet. This work was supported by CERN EP R&D on Experimental Technologies (WP8 Detector Magnets).

Appendix. Theory of an ideal flux pump

A flux pump switches between the charging and redistribution phase. In a full-wave flux pump this is achieved by two secondary circuits of which secondary coils are coupled in the opposite directions to the primary coil. In the charging phase, the load current I_{load} increases in one secondary circuit. In the redistribution phase, the currents I_1 and I_2 are enclosed in their individual secondary circuits, while the load current is given by their difference $I_{\text{load}} = I_1 - I_2$. The electrical schematic of the flux pump during charging is shown in figure 1 and during redistribution is shown in figure A1.

We consider the AC current in the primary coil to be given by

$$I_p(t) = -I_0 \cos(\omega t). \tag{A.1}$$

The phase is chosen so that the magnetic flux in the transformer starts increasing immediately after the flux pump is switched on. We are considering here to have a current source instead of voltage source and no resistive losses.

In the charging phase current is added to the active loop of the secondary circuit as

$$-M\frac{\mathrm{d}I_p}{\mathrm{d}t} + L_s\frac{\mathrm{d}I_{\text{load}}}{\mathrm{d}t} + L_{\text{load}}\frac{\mathrm{d}I_{\text{load}}}{\mathrm{d}t} = 0 \tag{A.2}$$

together with an initial condition

$$I_{\text{load}}(\tau_r) = I_{\text{init}}\,, \tag{A.3}$$

where I_{init} represents the load current at the beginning of a new cycle. The parameter τ_r represents a redistribution time, which is zero for the first cycle. The charging phase ends when the current on the primary coil reaches a maximum which happens when the magnetic flux changes direction. We solve equation (A.1) for the load current increase during one charging phase:

$$\Delta I_{\text{load}} = \frac{MI_0}{L_s + L_{\text{load}}}\left[1 + \cos(\omega\tau_r)\right]\,, \tag{A.4}$$

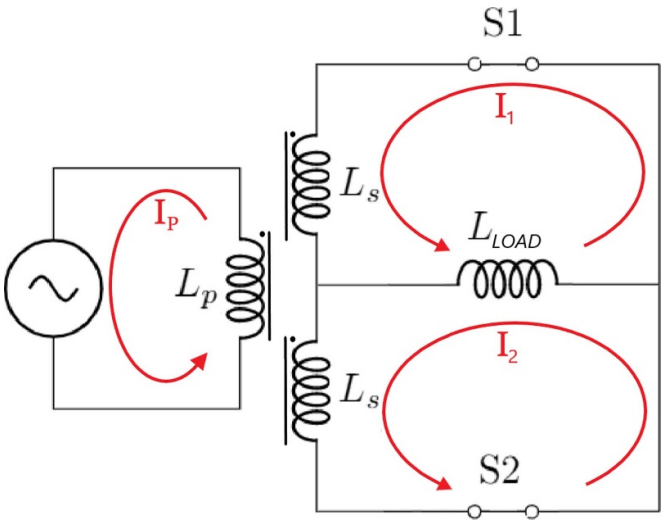

Figure A1. Electrical schematic of flux pump during current redistribution.

where $\cos(\omega\tau_r)$ equals $+1$ in the first cycle ($\tau_r = 0$). In an ideal case without losses, once the maximum current is reached, we do not need to enter a charging phase again. Therefore, the redistribution time $\tau_r = \pi/\omega$ and the ΔI_{load} increment will be zero in every subsequent cycle. In the case of losses during redistribution, equation (A.4) ties up together redistribution time and current loss during each redistribution cycle.

Next, the current is redistributed from one loop to another. We are interested in how long it takes to redistribute the current, so that we can determine the duration of the charging phase. The equations in this case are

$$-M\frac{\mathrm{d}I_p}{\mathrm{d}t} + L_s\frac{\mathrm{d}I_1}{\mathrm{d}t} + L_{\text{load}}\frac{\mathrm{d}\left(I_1 - I_2\right)}{\mathrm{d}t} = 0 \tag{A.5}$$

$$-M\frac{\mathrm{d}I_p}{\mathrm{d}t} + L_s\frac{\mathrm{d}I_2}{\mathrm{d}t} + L_{\text{load}}\frac{\mathrm{d}\left(I_2 - I_1\right)}{\mathrm{d}t} = 0 \tag{A.6}$$

with initial conditions

$$I_1\left(t_r\right) = I_{\text{load}}\ , \tag{A.7}$$

$$I_2\left(t_r\right) = 0\ . \tag{A.8}$$

The redistribution phase ends when all the current is redistributed to the second loop at $t = \tau_r$. Solving the above equations we obtain

$$I_1\left(\tau_r\right) = I_{\text{load}} - \frac{MI_0}{L_s}\left[1 - \cos\left(\omega\tau_r\right)\right]\ , \tag{A.9}$$

$$I_2\left(\tau_r\right) = -\frac{MI_0}{L_s}\left[1 - \cos\left(\omega\tau_r\right)\right]\ , \tag{A.10}$$

and the time required to redistribute I_1 to the second loop is given by

$$\tau_r = \frac{1}{\omega}\arccos\left(1 - \frac{I_{\text{load}}L_s}{I_0 M}\right)\ . \tag{A.11}$$

Therefore, the redistribution phase ends with currents $I_1 = 0$ and $I_2 = -I_{\text{load}}$ and we can continue with charging phase with the current I_2. From equation (A.11) we can determine maximum load current using redistribution time at the steady state as

$$I_{\text{load}}\left(\tau_r\right) = \frac{I_0 M}{L_s}\left(1 - \cos\left(\omega\tau_r\right)\right)\ . \tag{A.12}$$

A.1. Load current

The maximal current achievable by the superconducting flux pump is obtained from the redistribution behavior. We have two ways to derive the relation for the final form of the maximum current. The first way consists in calculating the amount of magnetic flux that we have to overcome during redistribution. To redistribute the current from one loop to another, we need to reduce the current in the loop from I_s to zero, and thus overcome the magnetic flux $\Delta\Phi = L_s I_s$. On the other hand we only have the magnetic flux $\Delta\Phi = M\Delta I_p$ in our disposal. If we have reached the maximum current $I_s = I_{\text{maxload}}$, all the magnetic flux generated by the primary coil is used in redistribution, and thus $\Delta I_p = 2I_0$ where I_0 is the value of the primary current in its amplitude. Therefore

$$I_{\text{maxload}} = \frac{2MI_0}{L_s}\ . \tag{A.13}$$

We obtain the same equation if we require that the redistribution time given by equation (A.11) leaves no time for further charging of the load. That is, when τ_r is equal to half of the AC current period $T/2$. Equation (A.11) shows that at zero load current $\arccos(1)$ and at maximum load current $\arccos(-1)$, and therefore we obtain again equation (A.13).

To derive I_{load} as a function of time, equation (A.4) is substituted with the redistribution time τ_r of equation (A.11) to obtain the current gain in a half period for full-wave rectifier as a function of I_{load} as

$$\Delta I_{\text{load}} = \frac{MI_0}{L_s + L_{\text{load}}}\left(2 - \frac{I_{\text{load}}L_s}{I_0 M}\right). \tag{A.14}$$

Let's look at the load current evolution (summation of ΔI_{load}) after the first few cycles

$$\begin{aligned}
n = 1: &\quad \frac{2MI_0}{L_s + L_{\text{load}}}\ ,\\
n = 2: &\quad 2\frac{2MI_0}{L_s + L_{\text{load}}} - \frac{2MI_0L_s}{\left(L_s + L_{\text{load}}\right)^2}\ ,\\
n = 3: &\quad 3\frac{2MI_0}{L_s + L_{\text{load}}} - 3\frac{2MI_0L_s}{\left(L_s + L_{\text{load}}\right)^2}\\
&\quad + \frac{2MI_0L_s^2}{\left(L_s + L_{\text{load}}\right)^3}\ ,\\
n = 4: &\quad 4\frac{2MI_0}{L_s + L_{\text{load}}} - 6\frac{2MI_0L_s}{\left(L_s + L_{\text{load}}\right)^2}\\
&\quad + 4\frac{2MI_0L_s^2}{\left(L_s + L_{\text{load}}\right)^3} - \frac{2MI_0L_s^3}{\left(L_s + L_{\text{load}}\right)^4}\ .
\end{aligned}$$

By using Newton's binomial formula, the load current in the nth period is

$$\begin{aligned} I_{\text{load}}(n) = & \frac{2MI_0}{L_s}\left[\binom{n}{1}\frac{L_s}{L_s+L_{\text{load}}}\right. \\ & -\binom{n}{2}\left(\frac{L_s}{L_s+L_{\text{load}}}\right)^2 \\ & \left.+\cdots-(-1)^n\binom{n}{n}\left(\frac{L_s}{L_s+L_{\text{load}}}\right)^n\right] \\ I_{\text{load}}(n) = & \frac{2MI_0}{L_s}\left[1-\left(\frac{L_{\text{load}}}{L_s+L_{\text{load}}}\right)^n\right] \end{aligned} \tag{A.15}$$

with $n = 2ft$ in the case of a full-wave rectifier, where f is the frequency of the alternating current, we obtain equation (1). However, in case of losses this result is not valid and we should replace factor 2 with $(1-\cos(\omega\tau_r))$ to account for charging required to overcome the losses at the nominal current:

$$\begin{aligned} I_{\text{load}}(t) = & \frac{I_0 M}{L_s}(1-\cos(\omega\tau_r)) \\ & \cdot\left[1-\left(\frac{L_{\text{load}}}{L_s+L_{\text{load}}}\right)^{2ft}\right]. \end{aligned} \tag{A.16}$$

For a different current waveform (e.g. square or triangular wave), we can express all relations in terms of the total magnetic flux change $\Delta\Phi$ as

$$I_{\text{maxload}} = \frac{\Delta\Phi}{L_s}, \tag{A.17}$$

$$\tau_r = \frac{1}{\omega}\arccos\left(1-\frac{2I_{\text{load}}L_s}{\Delta\Phi}\right), \tag{A.18}$$

$$I_{\text{load}}(t) = \frac{\Delta\Phi}{L_s}\left[1-\left(\frac{L_{\text{load}}}{L_s+L_{\text{load}}}\right)^{2ft}\right]. \tag{A.19}$$

A.2. Load voltage

The induced voltage across the magnet during charging is

$$V_{\text{load}}(t) = L_{\text{load}}\frac{\mathrm{d}I_{\text{load}}(t)}{\mathrm{d}t}. \tag{A.20}$$

Here we can immediately notice that the voltage during redistribution is equal to zero in the case of ideal rectification (zero resistance). This is because the current does not change during redistribution. However, for a real flux pump current decreases with time due to resistive losses in the secondary circuit. The load voltage during charging in equation (4) is derived from equations (A.1) and (A.20) as

$$V_{\text{load}}(t) = \frac{ML_{\text{load}}I_0}{L_s+L_{\text{load}}}\sin(\omega t), \tag{A.21}$$

where $t\in(\tau_r,\pi/\omega)$. However, in a realistic case the phase shift between load current and voltage is not exactly $\pi/2$. Therefore, the final result is

$$V_{\text{load}}(t) = \frac{ML_{\text{load}}I_0}{L_s+L_{\text{load}}}\cos(\omega t-\phi). \tag{A.22}$$

ORCID iDs

Róbert Jurčo https://orcid.org/0009-0005-3908-4947
Anna Vaskuri https://orcid.org/0000-0003-1246-4550
Benoit Curé https://orcid.org/0000-0002-8978-5267
Alexey Dudarev https://orcid.org/0000-0002-8713-8162
Matthias Mentink https://orcid.org/0000-0001-9769-0578

References

[1] ten Kate H 2010 *Int. J. Mod. Phys.* A **25** 2933–54
[2] van de Klundert L J M and ten Kate H H J 1981 *Cryogenics* **21** 195–206
[3] van de Klundert L J M and ten Kate H H J 1981 *Cryogenics* **21** 267–77
[4] Barkov L M, Bashtovoy N S, Karpov S V, Okhapkin V S, Ruban A A, Smakhtin V P, Snopkov I G and Zhuravkov I V 1999 *IEEE Trans. Appl. Supercond.* **9** 4585–90
[5] Mulder G B J, ten Kate H H J, Krooshoop H J G and van de Klundert L J M 1991 *IEEE Trans. Magn.* **27** 2333–6
[6] Coombs T A *et al* 2016 *IEEE Trans. Appl. Supercond.* **27** 1–6
[7] Wang W *et al* 2022 *Superconductivity* **3** 100022
[8] Bai Z, Yan G, Wu C, Ding S and Chen C 2010 *Cryogenics* **50** 688–92
[9] Bai Z, Chen C, Wu Y and Zhen Z 2011 *Cryogenics* **51** 530–3
[10] Fu L *et al* 2021 *IEEE Trans. Appl. Supercond.* **31** 9500805
[11] Bai Z, Cui X and Ma C 2021 *IEEE Trans. Appl. Supercond.* **31** 4602806
[12] Zhang Y *et al* 2020 *IEEE Trans. Appl. Supercond.* **30** 5000305
[13] Yang Z *et al* 2022 *IEEE Trans. Appl. Supercond.* **32** 5500405
[14] Pantoja A, Jiang Z, Badcock R A and Bumby C W 2016 *IEEE Trans. Appl. Supercond.* **26** 4805208
[15] Hamilton K, Pantoja A E, Storey J G, Jiang Z, Badcock R A and Bumby C W 2018 *IEEE Trans. Appl. Supercond.* **28** 5205705
[16] Ma J *et al* 2017 *Supercond. Sci. Technol.* **31** 015018
[17] Geng J *et al* 2019 *Supercond. Sci. Technol.* **32** 074004
[18] Geng J and Coombs T A 2016 *Supercond. Sci. Technol.* **29** 095004
[19] Geng J, Bumby C W and Badcock R A 2020 *Supercond. Sci. Technol.* **33** 045005
[20] Leuw B, Geng J, Rice J H P, Moseley D A and Badcock R A 2022 *Supercond. Sci. Technol.* **35** 035009
[21] Geng J, Brooks J M, Bumby C W and Badcock R A 2022 *Supercond. Sci. Technol.* **35** 025018
[22] Oomen M P, Leghissa M, Ries G, Proelss N, Neumueller H-W, Steinmeyer F, Vester M and Davies F 2005 *IEEE Trans. Appl. Supercond.* **15** 1465–8
[23] Klaassen D 2022 *CERN Technical Report* 2825574 v.1 (CERN) (available at: https://edms.cern.ch/nav/D:2825574:V1/D:2825574:V1)
[24] Fiorillo F *et al* 2016 *Wiley Encyclopedia of Electrical and Electronics Engineering* (Wiley) pp 1–42

[25] Transformer S, Toroidal Transformer—Open Standard open toroidal transformer, primary 2 × 115 VAC and 2 secondaries *Datasheet* (available at: www.st-t.pl/en)
[26] Bykovskiy N 2020 BabyIAXO design update *ATLAS+ Detector Magnets R&D Team Meeting at CERN (9 June 2020)*
[27] Vaskuri A *et al* 2023 *IEEE Trans. Appl. Supercond.* **33** 4500506
[28] Weiss J D *et al* 2017 *Supercond. Sci. Technol.* **30** 014002
[29] Mulder T *et al* 2019 *CERN Technical Report* 2305882 v.1 (CERN) (available at: https://edms.cern.ch/nav/D:2305882:V1/D:2305882:V1)
[30] Wimbush S and Strickland N 2014 Critical current characterisation of Sumitomo new type H DI-BSCCO® superconducting wire *Figshare, Dataset* (https://doi.org/10.6084/m9.figshare.1112565.v8)
[31] Wimbush S C, Strickland N M and Long N J 2015 *IEEE Trans. Appl. Supercond.* **25** 6400105 1–5